J. Phys. Chem. A **2000,** *104,* 2695−2705

Rate Coefficients for Reaction of OH with Acetone between 202 and 395 K

M. Wollenhaupt, S. A. Carl,[†] A. Horowitz,[‡] and J. N. Crowley*

Max-Planck-Institut für Chemie, Division of Atmospheric Chemistry, Postfach 3060, D-55020 Mainz, Germany

Received: October 20, 1999; In Final Form: January 20, 2000

The kinetics of the title reaction were investigated between 202 and 395 K and at 20, 50, and 100 Torr of Ar or N_2 bath gas using pulsed laser photolysis (PLP) generation of OH combined with both resonance fluorescence (RF) and laser-induced fluorescence (LIF) detection. OH was generated either by the sequential 439 nm, two-photon dissociation of NO_2 in the presence of H_2, or by HONO photolysis at 351 nm. The accuracy of the rate constants obtained was enhanced by optical absorption measurements of acetone concentrations both before and after the photolysis reactor. The temperature dependence is not described by a simple Arrhenius expression but by k_1 (202−395 K) = $8.8 \times 10^{-12} \exp(-1320/T) + 1.7 \times 10^{-14} \exp(423/T)$ cm^3 s^{-1}, indicating that a simple H atom abstraction may not be the only reaction mechanism. The estimated total error (95% confidence) associated with the rate coefficient derived from this expression is estimated as 5% and is independent of temperature. The curvature in the Arrhenius plot results in a significantly larger rate coefficient at low temperatures than obtained by extrapolation of the previous measurement and implies greater significance for the reaction with OH as a sink for acetone in the upper troposphere than presently assumed.

1. Introduction

The OH radical is the primary initiator of oxidation in the troposphere and its concentration determines the lifetimes, and thus the abundance, of most naturally and anthropogenically emitted chemical species[1] including CH_4 and also nonmethane hydrocarbons.

The OH-initiated degradation of some alkanes, especially propane, which is released into the troposphere mainly as a result of industrial activity, leads to formation of photochemically active, oxygenated organic trace gases including acetone, $CH_3C(O)CH_3$,[2,3] as does the reaction of both OH and O_3 with some alkenes and several naturally occurring terpenes.[4] Other sources of acetone are thought to be emissions from vegetation and biomass burning.[5−7]

The degradation of acetone, either via photolysis or reaction with OH, leads to the formation of peroxy radicals that can react with NO_2 to form peroxyacetyl nitrate (PAN), which plays an important role in the transport of NO_x, and thus in O_3 formation in remote regions. Although it has been recognized for many years that acetone is an important trace constituent of the troposphere,[4,8] recent measurements of high levels of acetone and also of PAN in the free troposphere suggest that up to 50% of PAN formation in the middle and upper troposphere may arise via acetone degradation. This highlights the role of acetone in contributing to the abundance of HO_x in the upper troposphere where OH formation via the photolysis of ozone in the presence of water vapor is limited by the low water vapor concentrations.[9−12] Indeed, if present at the several hundred pmol/mol level, the rate of HO_x production from acetone degradation may exceed that resulting from O_3 photolysis by a factor of 2−3.[13−16] The major fate of acetone in the mid and upper troposphere is believed to be photolysis, with removal by reaction with OH being the dominant loss process for the lower troposphere.

The aims of this study were to extend the available kinetic data on the reaction of OH with acetone ($CH_3C(O)CH_3$) to temperatures that prevail in the upper troposphere. At the onset of this research data were available between ≈440 and 240 K.

$$OH + CH_3C(O)CH_3 \rightarrow \text{products} \qquad (1)$$

2. Experimental Section

In the course of this experimental study, two different methods of formation and detection of OH were employed. In both cases pulsed laser photolysis (PLP) of suitable precursors served to generate OH on short time scales compared to their removal by reaction, while both resonance fluorescence (RF) and pulsed laser-induced fluorescence (PLIF) were used to detect it. The PLP−RF experimental setup has been described previously[17,18] and is only briefly recounted here. The PLP−PLIF setup has been recently commissioned and is reported in detail for the first time.

2.1. PLP−RF. The PLP−RF experiments were carried out using a thermostated, Teflon-coated stainless steel reaction vessel. The pulsed photolysis beam at 439.44 used to generate OH (see below) was provided by a Nd:YAG pumped dye-laser operating at 10 Hz with coumarin 120 dye. The laser emission was expanded to a collimated beam of about 5 mm diameter and passed through three irises of ≈4 mm diameter before entering the reaction vessel through a quartz window at the Brewster angle. Pulse energies were monitored with a Joule meter placed behind the exit Brewster window. OH radicals were excited by a microwave-powered discharge lamp and their fluorescence detected at right angles to both the axis of propagation of the laser beam and the microwave lamp by a photomultiplier operating in photon counting mode, which was screened by a 309 ± 5 nm interference filter. Between 1000 and 5000 decays profiles were averaged to improve signal-to-noise ratios. The temperature of the gas at the intersection of the microwave lamp and laser beam was determined to an

---

[†] Now at: Department of Chemistry, University of Leuven, Celestijnenlaan 200F, B-3001 Leuven, Belgium.

[‡] Permanent address: Soreq Research Centre, Yavne 81800, Israel.

10.1021/jp993738f CCC: $19.00

accuracy of better than 2 K with a constantan–alumel thermocouple. All experiments were carried out in 20 Torr Ar.

Generation of OH. In the PLP–RF experiments, OH generation is initiated by the photolysis of NO_2 according to the following scheme.[19]

$$NO_2 + h\nu\ (439.44\ \text{nm}) \rightarrow NO_2^* \qquad (2)$$

$$NO_2^* + h\nu\ (439.44\ \text{nm}) \rightarrow NO_2^{**} \qquad (3)$$

$$NO_2^{**} \rightarrow NO + O(^1D) \qquad (4a)$$

$$NO_2^{**} \rightarrow NO + O(^3P) \qquad (4b)$$

$$O(^1D) + H_2 \rightarrow OH + H \qquad (5)$$

$$H + NO_2 \rightarrow OH + NO \qquad (6)$$

In all experiments the total pressure was 20 Torr, and the NO_2 concentration was held constant at $\approx 5 \times 10^{14}$ cm^{-3} (occasionally determined optically), with the H_2 concentration at about 2×10^{16} cm^{-3}. Under these conditions, OH generation, the rate of which is limited by reaction 6, is complete within about 30 μs after the laser pulse. The relaxation time for the vibrationally excited OH formed in reactions 5 and 6 is $\approx$60 μs.[19] Typically, laser fluences of $\approx$20–40 mJ cm^{-2} were used to generate between $\approx 2 \times 10^{11}$ and 1×10^{12} OH cm^{-3}.

The 248 nm photolysis of either HNO_3 or H_2O_2 as OH source was judged to be unsuitable due to the broad, partially dissociative absorption of $CH_3C(O)CH_3$ that extends from $\approx$210 to 340 nm.

$$CH_3C(O)CH_3 + h\nu\ (248\ \text{nm}) \rightarrow CH_3 + CH_3CO \qquad (7)$$

Calculations show that under typical experimental conditions (e.g., $[CH_3C(O)CH_3] = 1 \times 10^{16}$ cm^{-3}, $[OH]_0 = 1 \times 10^{12}$ cm^{-3}), the loss of OH is significantly enhanced by the presence of CH_3 and CH_3CO, both of which have large rate constants ($> 5 \times 10^{-11}$ cm^3 s^{-1}) for reaction with OH.[20,21]

2.2. PLP–PLIF. The PLP–PLIF experiments (see Figure 1) were carried out using a double-jacketed, thermostated, quartz reactor of volume $\approx$500 cm^3. Gas mixtures entered the reactor $\approx$15 cm upstream of the photolysis region to ensure thermal equilibrium with the walls of the vessel and were pumped out through ports in the baffle arms and in front of the fluorescence collection lens. The cell was thermostated to the desired temperature by circulating either water or ethanol from a cryostat (Huber Unistat 390 W). The ends of the baffle arms and the lens support were kept warm using resistive heating wire to prevent condensation of ambient water vapor when working at low temperatures. The pressure in the cell, monitored with 10, 100, and 1000 Torr capacitance manometers, was held constant at 50 or 100 Torr, using either Ar or N_2 as bath gases. Typical flow rates, regulated using calibrated mass flow controllers, were between 250 and 500 sccm, resulting in linear gas velocities in the reaction cell of $\approx$40 cm s^{-1}, ensuring that a fresh gas sample was photolyzed at each laser pulse and prevented buildup of products.

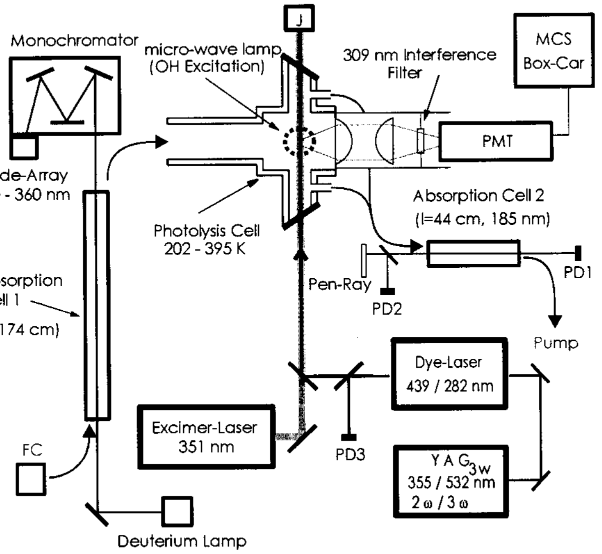

Figure 1. PLP–PLIF and PLP–RF experimental setup. PMT = photomultiplier, FC = flow controller. PD1 and PD2 are photodiodes to measure extinction of light by acetone (PD1) and monitor fluctuations in analysis light intensity (PD2). PD3 is used to monitor the shot-to-shot variation in the excitation laser intensity. J = Joule meter. Both 174 and 44 cm optical absorption cells are at room temperature. Signals from the PMT are amplified and counted by a multichannel scaler (MCS) for the PLP–RF experiments or integrated by boxcar integrator.

The pulsed emission from the excimer photolysis laser (Lambda Physik Lextra 50) and the YAG-pumped, frequency-doubled dye laser used as excitation source (Quantel Brilliant B, Lambda Physik Scanmate/ScanmateUV with KDP crystal) were coupled onto the same axis using a dielectric mirror before propagating in the same direction into the reaction volume through quartz windows at the Brewster angle. The Brewster-angle entrance and exit windows were located behind a series of $\approx$0.8 cm baffles to reduce stray light from the photolysis and excitation lasers. Fluorescence was gathered by a $f = 1.4$ telescopic arrangement and focused onto the active area of a photomultiplier, which was screened by a 309 ± 5 nm interference filter and a BG26 glass cutoff filter. The temperature of the gas mixture in the cell was measured using a J-Type thermocouple that could be inserted into the reaction volume where the focus of the telescopic lens system and the laser beams cross. The laser fluences were monitored by a calibrated Joule meter located behind the exit Brewster window.

The timing of the excimer laser and the dye laser was controlled using a digital delay generator (Stanstead Research Systems DG 535) interfaced to a PC. The experiment was conducted in scan mode, so that the delay between the lasers was incremented after each laser pulse, i.e., at 10 Hz. Typically, 10 data points were measured before the excimer laser fired, and 50 points afterward, resulting in a scan time of 6 s. This short time scan ensures that long time (>6 s) fluctuations in laser intensities do not result in a distortion of the decay profile. The PMT signal measured before the excimer was triggered (i.e., in the absence of OH) was used to correct the OH fluorescence signal for scattered light from the excitation laser. In addition, a small amount of the dye-laser light was split off and its relative intensity measured using a photodiode. This shot-to-shot relative variation in laser intensity was recorded and used to normalize the fluorescence signals. Typically, 20 scans (120 s) were then sufficient to map the OH profile. The PMT signals were recorded by a gated boxcar integrator (Stanstead Research Systems SR250) $\approx$0.1 μs after the excitation laser pulse over a gate width of $\approx$1 μs. Occasionally, the first point measured after the excimer laser pulse was slightly influenced by stray light from the excimer laser and was rejected in the analysis of the OH decay.

Generation and Detection of OH. In the PLP-LIF experiments, OH was generated in the 351 nm (XeF excimer laser) photolysis of HONO. Typically, $\approx 1 \times 10^{13}$ cm^{-3} of HONO were photolyzed at a laser fluence of $\approx$20 mJ cm^{-2} to generate

$\approx(5-10) \times 10^{10}$ cm^{-3} of OH. HONO was made in situ by passing a 5 sccm flow of HCl diluted in N_2 ($\approx$1‰) over a stirred bed of $NaNO_2$ crystals ($\approx$50 g). The HONO thus formed contained a similar amount of NO and $\approx$3–5% NO_2 impurity but has the advantage of containing minimal amounts of water vapor, which could complicate experiments at the lowest temperatures of this study. This HONO source provided a stable, reproducible flow of HONO for several weeks. There is some indirect evidence that the photolysis of HONO at wavelengths close to 350 nm can lead to H atom formation, which can potentially complicate investigations of OH kinetics if the H atoms can react with NO_2 impurity to slowly generate OH.[22]

$$\mathrm{HONO} + h\nu\ (351\ \mathrm{nm}) \rightarrow \mathrm{OH} + \mathrm{NO} \qquad (8a)$$

$$\rightarrow \mathrm{H} + \mathrm{NO_2} \qquad (8b)$$

Experiments were therefore carried out in which H atom formation in the 351 nm photolysis of HONO was directly observed using resonance fluorescence at 121.6 nm (Lyman α). In this case the microwave discharge lamp was run with "pure" He, and the baffled connection between the microwave lamp and the photolysis cell was purged with a mixture of O_2 and Ar as filter for O atom and N atom emissions.[23] The system was calibrated for H atom sensitivity by photolyzing known concentrations of CH_3SH with a measured fluence at 248 nm, where the quantum yield for H atom formation is unity.[24] A small correction was applied for the attenuation of Lyman α by the CH_3SH. The sensitivity to H atoms is not significantly reduced in the presence of HONO as the HONO source is dry, and the low concentrations of HONO (and NO impurity) do not significantly attenuate the Lyman α radiation. This could be confirmed by photolyzing the CH_3SH at 284 nm in the presence of the HONO. The sensitivity was determined as 3×10^{-7} counts per second per H atom, resulting in a detection limit of better than 5×10^{8} cm^{-3}. We were unable to detect H atoms, and therefore, on the basis of measured laser fluences at 351 nm and the optically determined concentration of HONO, we set an upper limit of $\approx$1% for the quantum yield of H atom formation at 351 nm.

Fluorescence from OH was detected following excitation (pulse energy <1 mJ cm^{-2}) of the $A^2\Sigma$ ($v = 1$) ← $X^2\Pi$ ($v = 0$), Q_{11} (1) transition at 281.997 nm. Identical results were obtained by exciting at 282.254 nm (P_{11} (1)) and 282.150 nm (Q_{11} (2)).[25] Laser radiation at these wavelengths was provided by pumping rhodamine 6G dye at 532 nm with the second harmonic of the YAG laser (6 ns, 400 mJ) and frequency doubling the emission at $\approx$560 nm. The sensitivity of this setup to OH was established by photolysis of a known, optically measured concentration of HONO, with a known laser fluence. The detection limit in the absence of $CH_3C(O)CH_3$ was found to be $\approx 10^8$ cm^{-3} for a S/N = 1 (20 scans), which, in the presence of 10^{16} cm^{-3} of $CH_3C(O)CH_3$ was degraded by approximately 1 order of magnitude due to quenching of OH ($A^2\Sigma$).

To select the most suitable wavelength for OH excitation, and to completely characterize the newly commissioned PLIF system, experiments were undertaken to measure the fluorescence excitation spectrum (281.1–282.9 nm) of OH in 50 Torr Ar bath gas. The experiment was thus run in a synchronous scan mode, in which the wavelength of the excitation laser was scanned at a fixed rate ($\approx$0.4 nm/min) and OH fluorescence (excited at a fixed delay after the excimer laser) was collected at 10 Hz rate, averaged, and divided into 150 wavelength bins.

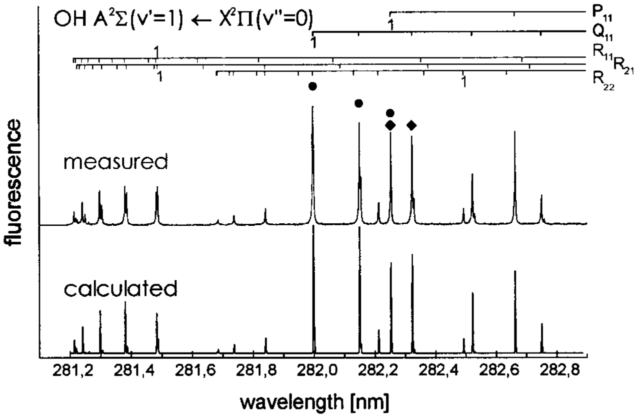

Figure 2. PLIF excitation spectrum of OH between 281.2 and 282.8 nm. The relative fluorescence intensity has been normalized for the wavelength-dependent variations in the fluence of the excitation laser. Rotational lines marked by solid circles were used for the kinetic measurements; the pair marked with solid diamonds was used for the calculations of the OH rotational temperature.

The resulting spectrum at 298 K, which is normalized for wavelength-dependent variations in the excitation laser energy is displayed in Figure 2, along with a calculated excitation spectrum for the same temperature. The OH A–X (1,0) excitation spectra at a given temperature were calculated assuming a Boltzmann distribution for population of the rotational levels in the $X^2\ \Pi$ ($v' = 0$) electronic ground state. The energies of the $A^2\Sigma$ ($V' = 1$, J') and $X^2\Pi$ ($V'' = 0$, J'') rotational levels and corresponding transition probabilities were taken from Dieke and Crosswhite.[25] Figure 2 shows that the 281.997 nm transition is the most intense, is well separated from other rotational lines, and was therefore selected for the great majority of the measurements.

The above procedure was repeated at a higher spectral resolution for a reduced wavelength region (282.24–282.35 nm) that covered only two rotational lines, and at temperatures of 220–295 K. The resultant spectra were then compared to calculated temperature-dependent excitation spectra to derive the rotational temperature of OH $\approx$0.1 μs after its generation. This agreed to within 2 K with the in situ measured bath-gas temperature, showing that OH is properly thermalized under our experimental conditions and giving us confidence in the experimental procedure.

2.3. Concentration of $CH_3C(O)CH_3$ (PLP–RF and PLP-LIF). Special effort was made to accurately measure the concentration of $CH_3C(O)CH_3$, which is the parameter that most influences the final errors in the measured rate coefficients. Following several degassing cycles at 77 K, $CH_3C(O)CH_3$ was accurately mixed with Ar in a 6 or 10 L glass storage bulb, typically with a mixing ratio of close to 0.1. A variable flow of $CH_3C(O)CH_3$ was then measured by a flow controller that had been freshly calibrated for each new $CH_3C(O)CH_3$/Ar mixture, and mixed with the calibrated flow of Ar or N_2 that comprised the bulk of the bath gas. The main flow of Ar or N_2 was actively regulated to maintain a constant total flow and pressure. A first estimate of the $CH_3C(O)CH_3$ concentration was then made by calculating its fractional flow and the total pressure and temperature.

In the PLP–RF experiments, the concentration of $CH_3C(O)CH_3$ was determined by a combination of optical and manometric methods. For the optical measurements, the absorption of UV light (D_2 lamp) was determined in a separate cell of 174 cm optical path length, which was connected serially in flow prior to the photolysis cell and maintained at room temperature.

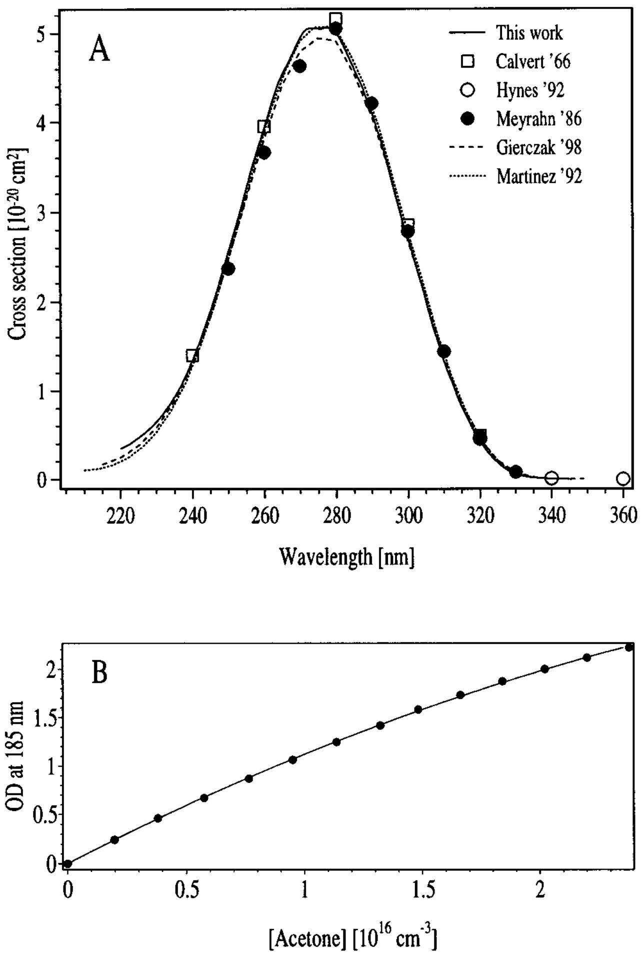

Figure 3. (A) UV-absorption spectrum of acetone at 296 K from this work, measured with diode array at a resolution of 0.3 nm. Previous studies at this temperature are also shown: Calvert,[26] Hynes,[28] Meyrahn,[27] Gierczak,[29] Martinez.[30] (B) Beer–Lambert plot of optical density measured at 185 nm due to a flowing mixture of acetone in Ar in the 44 cm absorption cell. The acetone concentration was determined by fitting to simultaneous measurements of absorption between 220 and 330 nm in the 174 cm cell using the diode array.

The entire absorption region of $CH_3C(O)CH_3$ between 220 and 380 nm was recorded by diode array spectroscopy, and concentrations were determined by least-squares fitting to UV-absorption spectra measured in this laboratory. A $CH_3C(O)CH_3$ reference spectrum was recorded using the same 174 cm absorption cell and monochromator/diode array arrangement, by measuring the absorption of static samples of pure $CH_3C(O)CH_3$ at several pressures between 0.35 and 4.4 Torr. The resultant spectrum between 220 and 340 nm (Figure 3A), was in excellent agreement with published data[26−30] and is expected to be accurate to within 3% at σ_{max} (≈270−280 nm).

This procedure worked well for the higher $CH_3C(O)CH_3$ concentrations at the beginning of each experiment. The quality of the least-squares fit of the optical density measurements to the UV spectrum of $CH_3C(O)CH_3$ was such that errors in $[CH_3C(O)CH_3]$ are estimated at $\leq 5\%$ (which includes errors in $CH_3C(O)CH_3$ cross sections). As the experiment progressed, and different $CH_3C(O)CH_3$ concentrations were used, drifts in the analysis light resulted in a distortion of the $CH_3C(O)CH_3$ spectrum and thus precluded accurate concentration measurement. For this reason, the optical determination of $CH_3C(O)CH_3$ was used to recalibrate the mixing ratio of $CH_3C(O)CH_3$ in its storage bulb. The correction factor was always less than 5%.

For the PLP−PLIF experiments, an additional optical cell (l = 44 cm), located at the exhaust of the photolysis cell was incorporated into the experiment. Here, the extinction of the 185 nm light from a low-pressure Hg lamp (Pen-Ray) could be monitored to calculate the $CH_3C(O)CH_3$ concentration. The 185 nm line was selected by an interference filter with high rejection of the 253.7 nm line, and detected by two photodiodes, one of which was used as reference to monitor fluctuations in the light intensity. The 44 cm optical absorption cell was enclosed in an evacuated stainless steel box to prevent absorption of the 185 nm light by ambient O_2 and H_2O vapor. The signals from the photodiodes were measured by picoammeters and integrated over 5 s to improve the signal-to-noise ratio. With this setup optical densities of 1×10^{-3} could easily be measured, with no loss of accuracy of the measurement over several hours. The calibration of the cross section of $CH_3C(O)CH_3$ at 185 nm was carried out by adding a flow of $CH_3C(O)CH_3$/Ar to the system and monitoring extinction in both the 174 cm (diode array) and 44 cm (185 nm Hg line) absorption cells. The $CH_3C(O)CH_3$ concentration in both cells was then derived by fitting a calibrated spectrum to the optical density measurements in the 174 cm cell. The relationship between $[CH_3C(O)CH_3]$ and the optical density at 185 nm is shown in Figure 3B. The curvature of this Beer−Lambert plot precludes calculation of the cross section, though at low $[CH_3C(O)CH_3] < 5 \times 10^{15}$ cm^{-3} an approximate cross section close to 2.75×10^{-18} cm^2 can be obtained by fitting a straight line through the first three points.

During the kinetic experiments, optical density measurements at 185 nm (typically between 0.2 and 2) were converted into absolute $CH_3C(O)CH_3$ concentrations using the calibration curve in Figure 3B. For these experiments, the potential interference by absorption of HONO, NO, or NO_2 at this wavelength was eliminated by measuring I_o (the intensity of the analysis light in the absence of $CH_3C(O)CH_3$) once stable flows of the HONO had already been established. Agreement in the concentration of $CH_3C(O)CH_3$ derived by both methods was always within 2% and indicated that no $CH_3C(O)CH_3$ was lost by condensation or reaction on the surface of the photolysis cell at any temperature.

2.4. Chemicals. $CH_3C(O)CH_3$ (Aldrich, 99.9%) was used after repeated degassing. Ar (Linde, 99.999%), N_2 (Linde, 99.999%), H_2 (Linde, 99.999%), HCl (≈1 ‰ in N_2), $NaNO_2$, and NO_2 (purchased as N_2O_4, Merck, 99.5%) were used without further purification.

3. Results

3.1. PLP−RF Experiments. All PLP−RF experiments were carried out under pseudo-first-order conditions, i.e., $[CH_3C(O)CH_3] \gg [OH]$. The decay of OH is then described by

$$[OH]_t = [OH]_0 \exp[-\{(k_1[CH_3C(O)CH_3] + k_9[NO_2] + d)t\}] \quad \text{(i)}$$

where $[OH]_t$ is the OH concentration at time t after the laser pulse, k_1 is the bimolecular rate coefficient for the reaction with $CH_3C(O)CH_3$, k_9 is the rate coefficient for reaction of OH with NO_2, and d is the rate coefficient for diffusion out of the reaction zone.

$$OH + NO_2 + M \rightarrow HNO_3 + M \quad (9)$$

The first-order decay rate, k', was obtained by nonlinear least-squares fitting of the OH decays (see Figure 4) and is related

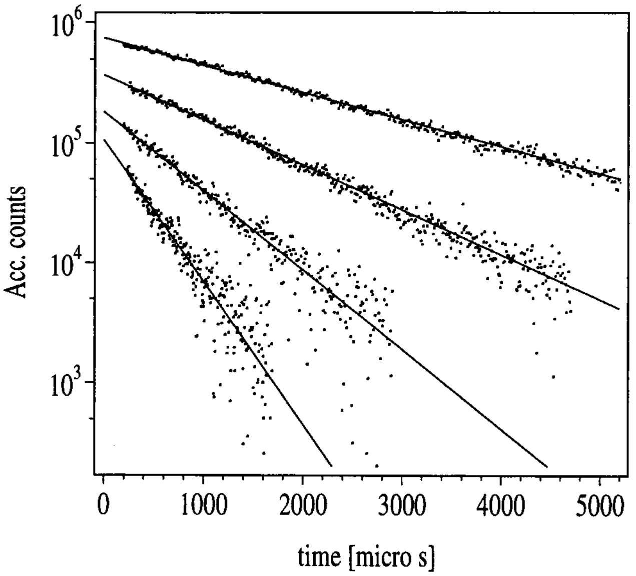

Figure 4. Decay of OH generated from the two-photon dissociation of NO_2 in the presence of H_2 and detected by RF. These particular data were gathered at a total pressure of 20 Torr (Ar bath gas) and at 298 K. The reduction in initial signal intensity is due to quenching of the $A^2\Sigma^+$ state of OH by acetone. The acetone concentration was (from upper to lower curves) 0, 1.98×10^{15}, 5.58×10^{15}, and 1.25×10^{16} cm^{-3}.

TABLE 1: Kinetic Data for OH + $CH_3C(O)CH_3$

T (K)	LIF/ RF	[acetone] (10^{15} cm^{-3})	a	p (Torr)	buffer gas	k' (s^{-1})[b]	$k_1 \pm 2\sigma$ (10^{-13} cm^3 s^{-1})
202	LIF	1.9−3.5	8	50	Ar	203−685	1.48 ± 0.05
209	LIF	2.9−10	6	50	Ar	626−2023	1.41 ± 0.04
218	LIF	3.7−21	18	50	N_2	386−3449	1.44 ± 0.02
220	LIF	4.4−21	7	50	Ar	375−3399	1.43 ± 0.02
221	RF	1.3−9.9	7	20	Ar	951−1831	1.25 ± 0.02
221	LIF	2.7−26	9	50	Ar	565−4539	1.45 ± 0.02
225	LIF	3.2−28	10	50	Ar	294−4358	1.40 ± 0.02
226	LIF	3.3−34	10	100	Ar	409−5413	1.36 ± 0.02
228	LIF	3.8−20	9	50	Ar	513−3206	1.37 ± 0.04
228	LIF	2.4−26	10	50	Ar	499−4519	1.38 ± 0.02
233	RF	2.2−9.8	8	20	Ar	820−2182	1.44 ± 0.03
233	RF	2.3−1.7	7	20	Ar	810−2295	1.25 ± 0.04
234	LIF	4.1−28	11	50	N_2	372−3818	1.28 ± 0.02
236	RF	2.2−9.5	6	20	Ar	826−2242	1.37 ± 0.03
236	RF	2.6−9.8	6	20	Ar	1358−2932	1.46 ± 0.04
236	LIF	4.3−28	10	100	N_2	397−3801	1.28 ± 0.02
237	LIF	5.2−29	9	100	Ar	379−4063	1.32 ± 0.02
244	RF	4.3−11.4	7	20	Ar	855−2607	1.51 ± 0.03
244	RF	4.8−13.7	9	20	Ar	835−2764	1.35 ± 0.03
247	RF	2.7−11.6	6	20	Ar	714−2450	1.41 ± 0.03
247	LIF	1.6−24	12	50	Ar	430−3796	1.42 ± 0.02
255	LIF	3.0−18	10	50	N_2	270−2726	1.36 ± 0.02
256	LIF	3.7−21	9	50	Ar	267−3179	1.38 ± 0.02
258	RF	2.5−12.9	7	20	Ar	675−2594	1.36 ± 0.03
261	RF	2.3−9.4	5	20	Ar	706−2195	1.48 ± 0.03
262	RF	2.4−15	8	20	Ar	799−2969	1.51 ± 0.03
267	LIF	2.2−25	11	50	Ar	331−3901	1.47 ± 0.01
274	LIF	2.3−2.5	11	50	Ar	137−4010	1.50 ± 0.02
281	LIF	2.1−25	11	50	Ar	132−4168	1.56 ± 0.02
289	LIF	2.1−24	11	50	Ar	206−4171	1.67 ± 0.02
295	LIF	2.9−15	6	50	Ar	238−3138	1.69 ± 0.04
298	RF	2.0−12.5	13	20	Ar	518−2804	1.77 ± 0.03
311	LIF	3.3−19	9	50	Ar	156−3494	1.96 ± 0.02
318	RF	1.4−8.7	8	20	Ar	447−2382	2.09 ± 0.04
321	LIF	2.5−17	10	50	N_2	179−3659	2.08 ± 0.02
321	LIF[c]	2.5−17	10	50	N_2	175−3720	2.08 ± 0.02
321	LIF[d]	4.9−10	3	50	N_2	173−2213	2.07 ± 0.05
332	LIF	2.8−16	9	50	Ar	186−3837	2.26 ± 0.03
344	LIF	2.3−16	10	50	N_2	175−4084	2.50 ± 0.03
355	LIF	3.5−18	10	50	Ar	148−4913	2.67 ± 0.03
360	RF	1.3−7.9	8	20	Ar	432−2654	2.85 ± 0.05
362	RF	1.7−7.8	8	20	Ar	476−2550	2.64 ± 0.07
395	RF	0.9−6.2	9	20	Ar	426−2630	3.54 ± 0.03

[a] Number of data points in plot of k' versus $[CH_3C(O)CH_3]$. [b] Range of measured pseudo-first order decay rates. Quoted errors are statistical only (2σ). [c] Excitation at 282.254 nm. [d] Excitation at 282.150 nm.

to the desired rate coefficient, k_1 as shown in eq ii.

$$k' = k_1[CH_3C(O)CH_3] + k_9[NO_2] + d \qquad \text{(ii)}$$

The decay rate of OH due to reaction with NO_2 appears as an intercept in the plot of k' versus $[CH_3C(O)CH_3]$. Efforts were therefore made to ensure that the concentration of NO_2 (which was maintained by flow controller) remained constant during the course of an experiment in which the decay of OH in various excess amounts of $CH_3C(O)CH_3$ was measured. The spectral deconvolution procedure showed that $[NO_2]$ was stable to ≈1% over such a measurement, which converts to a variation in the pseudo-first-order decay rate of only ± 60 s^{-1} in a total decay rate between 800 and 5000 s^{-1}, depending on the concentration of the $CH_3C(O)CH_3$. The observed small degree of scatter in the plots of k' versus $[CH_3C(O)CH_3]$ confirms this.

The kinetic results for the reaction of OH with $CH_3C(O)CH_3$ at 20 Torr total pressure (Ar bath gas) are summarized in Table 1, and selected plots of k' versus $[CH_3C(O)CH_3]$ (which define the rate constant according to eq ii are shown in Figure 5.

For experiments with high $CH_3C(O)CH_3$ a significant fraction of the $O(^1D)$ produced in reaction 4 will react with $CH_3C(O)CH_3$ and not H_2; i.e., for $[CH_3C(O)CH_3] = [H_2] = 1 \times 10^{16}$ cm^{-3}, 50% of the OH will originate from H-abstraction from $CH_3C(O)CH_3$ (assuming equal rate constants for $O(^1D)$ with H_2 and $CH_3C(O)CH_3$). To test for systematic errors related to this, experiments were carried out in which the initial concentration of H_2 was varied between 0 and 3.2×10^{16} cm^{-3} with $CH_3C(O)CH_3$ held constant at 5.5×10^{15} cm^{-3}. The first-order decay rate of OH was found to be invariant within the experimental scatter. Experiments were also carried out in which both NO_2 and the photon flux were varied, both resulting in changes in the initial OH concentration, and thus in the degree of conversion of $CH_3C(O)CH_3$ and product formation. Neither a factor of 2 increase in NO_2 (resulting in a factor of 2 change in OH) nor a factor of 2 increase in flux (resulting in a factor of 4 increase in OH) resulted in a change in the pseudo-first-order decay rate of OH for given conditions of initial $[CH_3C(O)CH_3]$ and total pressure. We also considered the possibility that OH formation in the reaction between $CH_3C(O)CH_3$ and $O(^3P)$ (formed at ca. twice the $[OH]_0$ concentration in reaction 4a) could reduce the apparent rate coefficient in the present study. However, given that the rate coefficient of $O(^3P) + CH_3C(O)CH_3$ is only $\approx 1 \times 10^{-14}$ cm^3 s^{-1} at 395 K[31] compared to a rate constant for $O(^3P) + NO_2$ of $\approx 8 \times 10^{-12}$ cm^3 s^{-1} at the same temperature[32] and that the relative concentrations of $CH_3C(O)CH_3$ to NO_2 were <30, then a maximum of ≈3% of the $O(^3P)$ will react with $CH_3C(O)CH_3$ to form OH at high temperatures. At low temperatures any influence of this reaction diminishes further as the rate coefficient for $O(^3P) + CH_3C(O)CH_3$ decreases ($E/R = 3000$/K) and that for $O(^3P) + NO_2$ increases ($E/R = -120$/K). In addition, a significant contribution of OH from this source would result in nonlinear plots of k' versus $[CH_3C(O)CH_3]$, which was not observed (Figure 5).

The temperature dependence of the rate coefficient for OH + $CH_3C(O)CH_3$ was investigated at 20 Torr and at temperatures between 221 and 395 K. The data are summarized in Table 1, and an Arrhenius plot of these data is displayed in Figure 6.

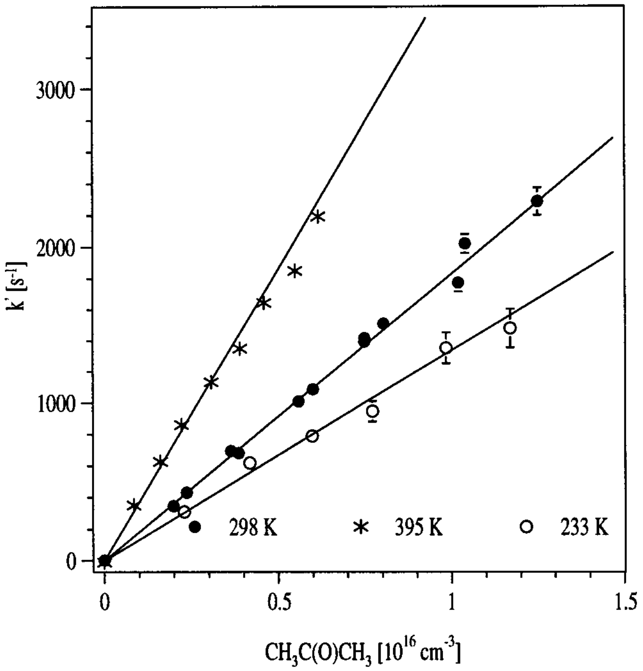

Figure 5. Plots of k' versus [$CH_3C(O)CH_3$] from LP−RF data obtained at 233, 298, and 395 K. The decay rate of OH in the absence of $CH_3C(O)CH_3$ ($\approx$400−800 s^{-1}; see Table 1) has been subtracted from each data set.

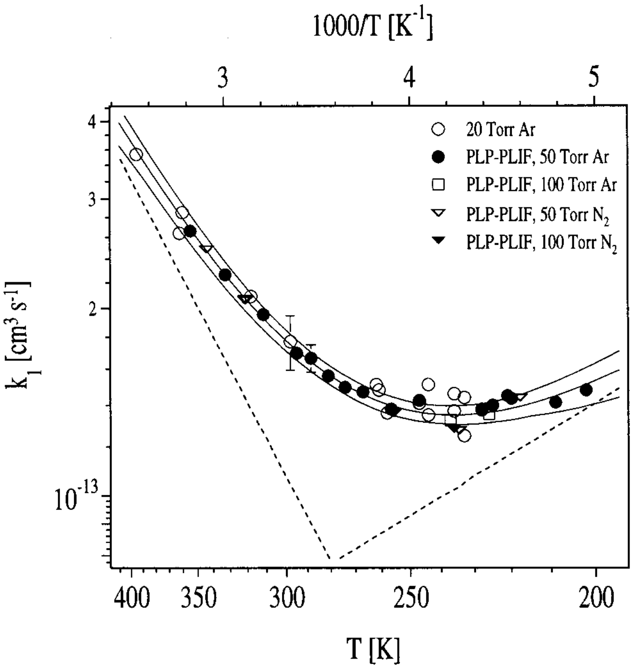

Figure 6. Arrhenius plot of all data obtained using both PLP−RF (○) and PLP−PLIF. The data are fit (central solid line) by a curve of the form $k(t) = A_1 \exp(-E_1/T) + A_2 \exp(E_2/T)$. The outermost solid curves represent the 95% confidence limits. The dotted lines are the individual contributions from the positive and negative temperature-dependent terms in $k(t)$. Representative error bars are shown for just one PLP−RF (10%) and one PLP−PLIF (5%) data point close to 300 K for clarity.

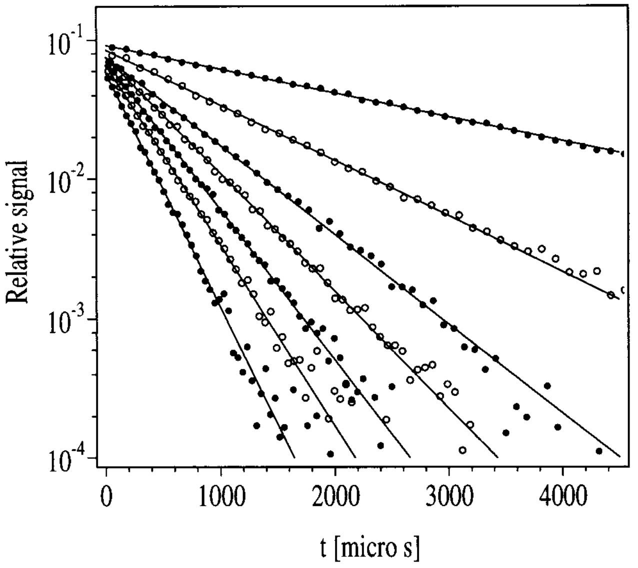

Figure 7. Decay of OH generated in the 351 nm photolysis of HONO at 237 K and 100 Torr (Ar bath gas) and detected by PLIF. The concentration of $CH_3C(O)CH_3$ was varied between 0 (upper decay) to 2.7 × 10^{16} cm^{-3} (lower decay).

3.2. PLP−PLIF Experiments. The PLP−PLIF investigations were carried out at pressures of either 50 or 100 Torr with both Ar and N_2 bath gases. Examples of OH decays measured by PLIF following its 351 nm pulsed generation from HONO are displayed in Figure 7. The decays are exponential over at least 3 half-lives and are described by

$$[OH]_t = [OH]_0 \exp[-\{(k_1[CH_3C(O)CH_3] + R_{sum} + d)t\}] \tag{iii}$$

where R_{sum} is the summed rate of loss of OH due to reaction with the HONO precursor and the NO and NO_2 impurities in the HONO source and is given by $R_{sum} = k_9[HONO] + k_{10}[NO_2] + k_{11}[NO]$. k_9, k_{10}, and k_{11} are the rate coefficients for reaction of OH with HONO, NO_2, and NO under the experimental conditions, respectively, and d is the rate constant for diffusion from the reaction zone.

$$OH + NO_2 + M \rightarrow HNO_3 + M \tag{9}$$

$$OH + HONO \rightarrow H_2O + NO_2 \tag{10}$$

$$OH + NO + M \rightarrow HONO + M \tag{11}$$

The rate coefficient for the reaction of OH with $CH_3C(O)CH_3$ is then derived from plots of k' versus [$CH_3C(O)CH_3$], where $k' = k_1[CH_3C(O)CH_3] + R_{sum} + d$. Such a data set is displayed in Figure 8 for experiments carried out at 234 K and 50 Torr of N_2 bath gas. The ordinate intercept is the sum of $R_{sum} + d$, and is $\approx$400 s^{-1} for this particular case.

In Figure 8 we also show the concentrations of $CH_3C(O)CH_3$ derived by optical measurements using both the 44 cm (185 nm) and 174 cm absorption cells (220−360 nm). The agreement is excellent and shows that no $CH_3C(O)CH_3$ is permanently lost to the cold surfaces of the quartz reactor. Only at temperatures less that 210 K and at higher $CH_3C(O)CH_3$ concentrations were deviations observed between the pre- and postphotolysis cell absorption measurements, indicating that $CH_3C(O)CH_3$ was being removed. Only those data were analyzed where the $CH_3C(O)CH_3$ concentrations (and thus the value of k_1) derived by these two methods agreed within a few percent. Figure 9 displays data measured at 354, 311, 274, and 235 K, exemplifying the high quality of the data obtained with this method at all temperatures. The measured OH-decay rates were found not to be significantly influenced by variation of the fluence of either the photolysis or excitation lasers by a factor of 6, or the flow rate. Also, excitation to different

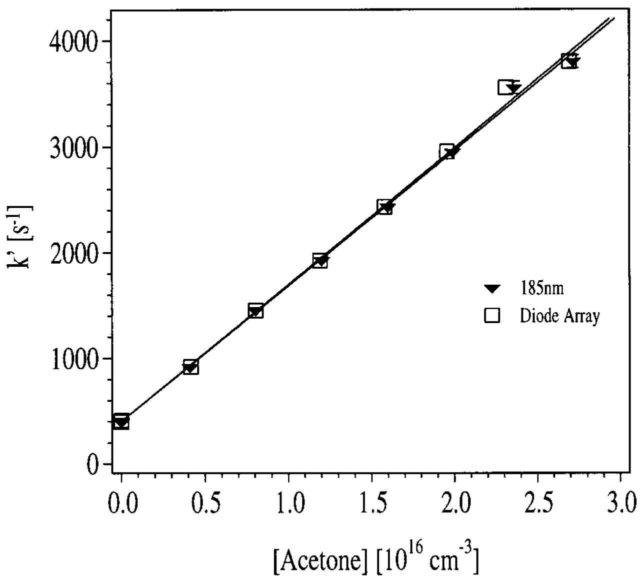

Figure 8. Plots of k' versus [$CH_3C(O)CH_3$] from the 237 K PLP−PLIF data displayed in Figure 7. The concentration of $CH_3C(O)CH_3$ as determined by extinction at 185 nm (squares) and diode array absorption spectroscopy (triangles) are in excellent agreement throughout the concentration range studied, showing that loss of $CH_3C(O)CH_3$ to the cold surface of the photolysis cell was insignificant. This particular data set gives $k_1 = (1.32 \pm 0.02) \times 10^{-13}$ cm^3 s^{-1} (statistical, 2σ errors).

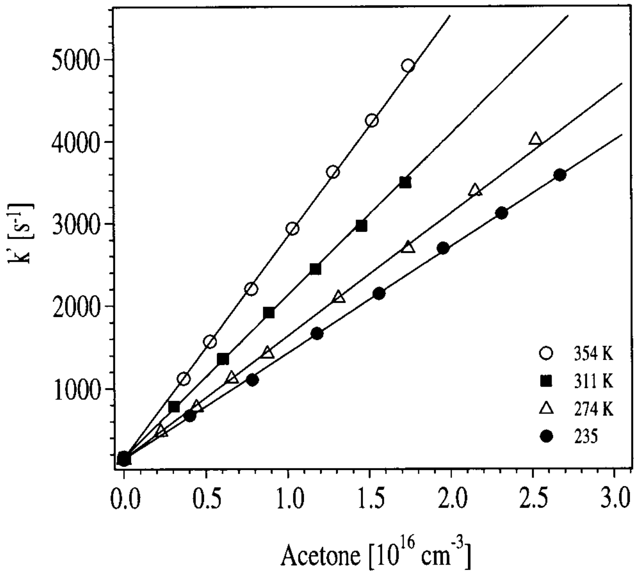

Figure 9. Plots of k' versus [$CH_3C(O)CH_3$] from PLP−PLIF data obtained at 234, 274, 311, and 355 K. The decay rate of OH in the absence of acetone (between ≈150 and 400 s^{-1}; see Table 1) has been subtracted from each data set.

rotational levels of OH $A^2\Sigma$ ($v = 1$) gave identical results. The complete data set is listed in Table 1 and displayed in Arrhenius format in Figure 6.

4. Discussion

A consistent set of data describing the kinetics of the reaction of OH with $CH_3C(O)CH_3$ reaction were obtained in the PLP−RF and PLP−PLIF experiments. The rate coefficient reveals no significant pressure dependence between 20 and 100 Torr, or bath gas dependence (Ar or N_2). The data obtained using PLP−PLIF is considered to be somewhat more accurate due to the dual-optical measurements of [$CH_3C(O)CH_3$] and the enhanced sensitivity to OH (cf. signal-to-noise ratios in Figures 4 and 7 and the relative scatter in Figures 5 and 9). Especially at low temperatures, where the loss rate of OH is significantly influenced by its reaction with NO_2, the precision of the PLP−RF measurements is reduced. I.e., the loss rate of OH in the absence of $CH_3C(O)CH_3$ is already 950 s^{-1}. For this reason, when deriving Arrhenius parameters by fitting to both data sets, we weighted the two sets of data accordingly. We estimate that the total errors in the PLP−PLIF experiments (including uncertainty in [$CH_3C(O)CH_3$]) is <5%. The comparable value for PLP−RF is ≈5−10%.

The high precision achieved in this study has revealed a distinct curvature in the Arrhenius plot for the reaction between OH and $CH_3C(O)CH_3$. Such curvature is often rationalized as a change of reaction mechanism as a function of temperature. One possibility is that at low temperatures the reaction no longer proceeds via a simple H atom abstraction but that an association complex is formed and is sufficiently stabilized to lead to product formation. The fact that no pressure dependence in the rate coefficient was observed implies that any association complex is rapidly thermalized by collisions with the buffer gas at pressures of 20 Torr or greater.

A likely mechanism involving an association complex is the electrophillic addition of OH to the carbonyl C atom, which is favored by the high electron density available within the carbonyl group. Similar mechanisms are known to exist for electrophillic attack of OH at other electron rich centers such as C=C double bonds and S atoms. Also, we note that the reactions of larger ketones with OH display curved Arrhenius plots and sometimes negative temperature dependencies[33] and that the concept of electrophillic addition of OH to the carbonyl group in ketones has previously been inferred.[34]

$$OH + CH_3C(O)CH_3 \rightarrow [(CH_3)_2C(O)OH]^{\#} \rightarrow \text{products} \quad (1)$$

The association complex, AC, $[(CH_3)_2C(O)OH]^{\#}$ can decompose by C−C bond fission to yield acetic acid ($CH_3C(O)OH$) and CH_3 radicals as products, or back to reactants. The formation of acetic acid and CH_3 from reaction 1 is thermodynamically feasible and indeed represents the most exothermic reaction channel (enthalpies of formation taken from ref 35):

$$OH + CH_3C(O)CH_3 \rightarrow H_2O + CH_3C(O)CH_2 \quad (\Delta H_r = -88\ \text{kJ/mol}) \quad (1a)$$

$$\rightarrow AC \rightarrow CH_3 + CH_3C(O)OH \quad (\Delta H_r = -108\ \text{kJ/mol}) \quad (1b)$$

Further exothermic reaction channels involve the decomposition of the association complex to form $CH_3OH + CH_3C(O)$ (reaction 1c), $CH_4 + CH_3CO_2$ (reaction 1d), or $H_2O + CH_3C(O)CH_2$ (reaction 1a).

$$OH + CH_3C(O)CH_3 \rightarrow AC \rightarrow CH_3OH + CH_3C(O) \quad (\Delta H_r = -48\ \text{kJ/mol}) \quad (1c)$$

$$\rightarrow AC \rightarrow CH_4 + CH_3CO_2 \quad (\Delta H_r = -105\ \text{kJ/mol}) \quad (1d)$$

$$\rightarrow AC \rightarrow H_2O + CH_3C(O)CH_2 \quad (\Delta H_r = -88\ \text{kJ/mol}) \quad (1e)$$

Pathways 1c−1e seem, however, unlikely to be significant as the rearrangements necessary involve three or four centered transition states and are probably energetically disfavored.

The temperature-dependent rate coefficient was fitted to an equation of the form

$$k(t) = A_1 \exp(-E_1/T) + A_2 \exp(E_2/T) \qquad \text{(iv)}$$

where A_1 and A_2 are the preexponential factors for the direct H-abstraction and for the pathway involving an association complex, respectively. Similarly, E_1 and E_2 are related to the activation energies for each mechanism. The data are well described throughout the temperature range covered by k_1 (202−395 K) = $(8.8 \pm 3.6) \times 10^{-12} \exp\{(-1320 \pm 163)/T\} + (1.7 \pm 0.9) \times 10^{-14} \exp\{(423 \pm 109)/T\}$ cm^3 s^{-1}, where the errors are 2σ as returned from the fit routine. The total error (at 95% confidence limit, see Figure 6) incurred when using this expression to calculate k_1 at any particular temperature covered by the present work is ≈5%.

Support for the hypothesis that the reaction can be described by a combination of H-abstraction and addition is provided by comparing the above equation to the data for reaction of OH with ethane (C_2H_6), which, like $CH_3C(O)CH_3$ has six equivalent C−H bonds. In this case the reaction is known to proceed via direct H-abstraction. The first Arrhenius term (direct abstraction), with $A_1 = 8.8 \times 10^{-12}$ cm^3 s^{-1} and $E_1/R = (1320 \pm 163)$/K is very similar to the expression recommended for the reaction of OH with ethane ($A = 8.7 \times 10^{-12}$ cm^3 s^{-1} and $E/R = (1070 \pm 100)$/K [32]), implying only a small influence of the adjacent carbonyl group on the C−H bond strength.

The data were also fitted to an equation of the form $k(t) = A^n \exp(-E/RT)$, i.e., with a temperature dependent preexponential factor. Although the temperature dependence of the data could be reproduced with this form of the Arrhenius equation, the curvature at low temperatures could not be reproduced with physically meaningful values of A and n (e.g., $A < 10^{-30}$, $n > 5$), and we prefer to represent the data with a double Arrhenius expression.

Having postulated that the reaction has two pathways, we can estimate their relative importance as a function of the temperature. The dashed lines in Figure 6 represent the individual contributions from both the H-abstraction and addition pathways between 400 and 200 K. Our results infer roughly equal contributions at 280 K. At $T = 210$ K, the association complex mechanism contributes some 90% of the overall rate coefficient. Similarly, at 400 K, the abstraction channel dominates with ≈90% contribution. Thus, by assuming that formation of $CH_3C(O)OH$ and CH_3 is the major decomposition channel for the association complex at low temperatures, we hypothesize that acetic acid is a major product of the OH-initiated oxidation of $CH_3C(O)CH_3$ in regions of the atmospheric characterized by low temperatures (see later).

4.1. Comparison with Previous Work. Along with the present data, Figure 10 presents the temperature-dependent data in the literature.[34,33] All the published, absolute measurements have used pulsed photolysis (flashlamp or laser) to generate OH and either resonance fluorescence, or laser-induced fluorescence, to detect it. A variety of photolytic OH precursors have been employed including H_2O ($\lambda > 165$ nm), HONO ($\lambda = 351$ nm), and NO_2/H_2 ($\lambda = 439.44$ nm).

The room-temperature rate coefficient measured by Le Calvé[33] is $(1.84 \pm 0.24) \times 10^{-12}$ cm^3 s^{-1}, in excellent agreement with the present determination $(1.73 \pm 0.09) \times 10^{-13}$ cm^3 s^{-1}. At $(2.16 \pm 0.16) \times 10^{-13}$ cm^3 s^{-1}, the room-temperature rate constant of Wallington and Kurylo[34] is slightly higher, and the results do not agree within the quoted 2σ uncertainties. A further, unpublished absolute rate coefficient determination at room temperature yielded values of $(2.3 \pm 0.3) \times 10^{-13}$ cm^3 s^{-1} in static mixtures at 50 Torr and $(2.0 \pm 0.70) \times 10^{-13}$ cm^3 s^{-1} in flowing mixtures at 100 Torr.[36]

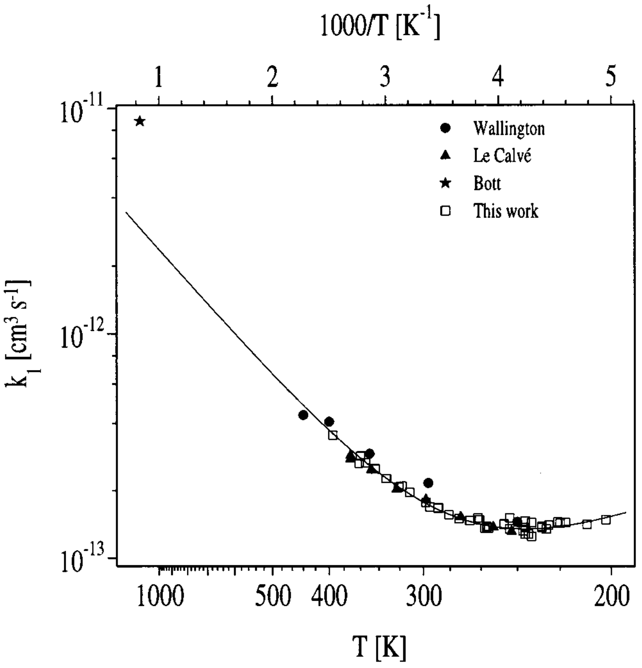

Figure 10. Arrhenius plot of absolute kinetic data published for OH + acetone. The fit is to the present data only.

Three room temperature relative rate studies have measured values of $\leq 5 \times 10^{-13}$ cm^3 s^{-1},[37] $(2.6 \pm 0.8) \times 10^{-13}$ cm^3 s^{-1},[38] and $(6.6 \pm 0.9) \times 10^{-13}$ cm^3 s^{-1}.[39] The use of more recently determined OH rate coefficients for the reference compounds (C_2H_4 for Kerr and Stocker,[38] n-C_6H_{14} for Chiorboli et al.[39]) has no significant influence on the final determination of k_1 from these studies, and the reason for the high value for OH + $CH_3C(O)CH_3$ in the latter study remains unclear. The literature data on the reaction of OH with $CH_3C(O)CH_3$ are summarized in Table 2.

Until now, the temperature dependence has been described by the single Arrhenius expressions listed in Table 2: The results of Wallington and Kurylo[34] indicates no curvature within the experimental uncertainty, though the data are considerably more scattered than in the present study. Despite this, we note that only the room temperature result of Wallington and Kurylo deviates significantly from the present results. Although Le Calvé et al.[33] chose to fit their data using a single Arrhenius expression, the precision of their work is sufficient to reveal a strong curvature. Indeed, their data are in very close agreement with those measured in the present study, throughout the range of overlap in temperature.

Further evidence that the temperature dependence of k_1 is not described by a simple Arrhenius expression is provided by the shock tube work of Bott and Cohen,[40] whose data indicate a rate coefficient at 1200 K of 8.8×10^{-12} cm^3 s^{-1} (see Figure 10).

4.2. Atmospheric Implications. The rate constant measured in the present study indicates that previous assessments of the role of reaction with OH as a sink for atmospheric $CH_3C(O)CH_3$ may have underestimated the relative importance of this reaction compared to photolysis in the upper troposphere. In this part of the atmosphere, both the low temperatures, which result in a rate coefficient for the reaction of OH with $CH_3C(O)CH_3$ that is greater than that previously recommended, and

TABLE 2: Summary of Data on OH + Acetone

ref	method	OH^- source	T range	$k_1{}^a$ ($cm^3\ s^{-1}$) (room temp)	A^e ($cm^3\ s^{-1}$)	E/R^e (K^{-1})
this work	absolute PLP−PLIF PLP−RF	HONO ($\lambda = 351$ nm) NO_2/H_2 ($\lambda = 439.4$ nm)	202−395	1.73 ± 0.09	8.8×10^{-12} 1.7×10^{-14}	1320 −423
34	absolute FP−RF	H_2O ($\lambda > 165$ nm)	240−440	2.16 ± 0.16	1.7×10^{-12}	600
33	absolute PLP−PLIF	HONO ($\lambda = 351$ nm)	243−372	1.84 ± 0.24	1.25×10^{-12}	651
36	absolute FP−RF	H_2O ($\lambda > 105$ nm)	298	$2.3 \pm 0.3^{b,c}$ 2.0 ± 0.70^{d}		
37	relative (to C_2H_4)	HONO (300−450 nm)	300	≤ 0.5		
38	relative (to C_2H_4)	HONO (350−450 nm)	300	2.6 ± 0.08		
39	relative (to n-C_6H_{14})	HONO (330−700 nm)	298	6.6 ± 0.09		
40	absolute shock tube	t-$(CH_3)_3COOH$	1200			

[a] Errors quoted are statistical only (2σ). [b] Estimated total errors of 15% reported. [c] Static gas mixtures. [d] Flowing gas mixtures. [e] Rate coefficient given by $k(T) = A \exp(-E/RT)$ except for the present work where $k(T) = A \exp(-E/RT) + A \exp(-E/RT)$.

the presence of partially oxidized hydrocarbons such as $CH_3C(O)CH_3$, which result in enhanced OH concentrations for a given solar flux, combine to enhance the relative importance of OH reaction to photolysis of $CH_3C(O)CH_3$. As shown by Gierczak et al.[29] and McKeen et al.[41] for ≈2 nmol/mol of $CH_3C(O)CH_3$, OH concentrations of up to 5 pmol/mol are expected. Using a rate coefficient of $k_1 = 8.4 \times 10^{-14}$ at 210 K, these authors derived a loss rate for reaction with OH of $\approx 1 \times 10^{-7}\ s^{-1}$, compared to $4 \times 10^{-7}\ s^{-1}$ for photolysis. The new rate constant at this temperature is $\approx 1.4 \times 10^{-13}$ at 210 K, resulting in a loss rate due to reaction 1, which contributes ≈30% to the overall sink.

In addition, we note that the speciation of the peroxy radicals formed in the oxidation of $CH_3C(O)CH_3$, and the efficiency of formation of HO_x may be modified. The photolysis of $CH_3C(O)CH_3$ results in the formation of both methyl- and acetylperoxy radicals (CH_3O_2 and $CH_3C(O)O_2$ respectively):

$$CH_3C(O)CH_3 + h\nu \rightarrow CH_3 + CH_3C(O) \qquad (12)$$

$$CH_3 + O_2 + M \rightarrow CH_3O_2 + M \qquad (13)$$

$$CH_3C(O) + O_2 + M \rightarrow CH_3C(O)O_2 + M \qquad (14)$$

In the upper troposphere, both peroxy radicals can react with NO to ultimately form HO_x:

$$CH_3C(O)O_2 + NO \rightarrow CH_3C(O)O + NO_2 \qquad (15)$$

$$CH_3C(O)O\ (+ O_2) \rightarrow CH_3O_2 + CO_2 \qquad (16)$$

$$CH_3O_2 + NO \rightarrow CH_3O + NO_2 \qquad (17)$$

$$CH_3O + O_2 \rightarrow HCHO + HO_2 \qquad (18)$$

$$HO_2 + NO \rightarrow OH + NO_2 \qquad (19)$$

$$HCHO + h\nu\ (+ O_2) \rightarrow 2\ HO_2 + CO \qquad (20)$$

From the above, we see that, given sufficient NO_x, the photolysis of a single molecule of $CH_3C(O)CH_3$ results in the formation of two HCHO, CO_2, and two OH radicals. As HCHO is also eventually converted to OH, a total of three to four OH radicals are generated per $CH_3C(O)CH_3$.[9] At the same time, five NO molecules are oxidized to NO_2, which can significantly contribute to O_3 formation in the upper troposphere.[42,43] In addition, the reaction of $CH_3C(O)O_2$ with NO_2 at low temperatures results in the formation of peroxyacetyl nitrate (PAN, $CH_3C(O)OONO_2$).[9]

$$CH_3C(O)O_2 + NO_2 + M \rightarrow CH_3C(O)O_2NO_2 + M \qquad (21)$$

At low levels of NO_x the reactions of CH_3O_2 and $CH_3C(O)O_2$ with HO_2 can gain importance:

$$CH_3O_2 + HO_2 \rightarrow CH_3OOH + O_2 \qquad (22)$$

$$CH_3C(O)O_2 + HO_2 \rightarrow CH_3C(O)OOH + O_2 \qquad (23a)$$

$$\rightarrow CH_3C(O)OH + O_3 \qquad (23b)$$

and can result in the formation of methyl peroxide (CH_3OOH), acetic acid ($CH_3C(O)OH$), and peracetic acid ($CH_3C(O)OOH$). The removal of $CH_3C(O)CH_3$ via H-abstraction by OH gives rise to the following chemistry:

$$OH + CH_3C(O)CH_3 \rightarrow H_2O + CH_3C(O)CH_2 \qquad (1a)$$

$$CH_3C(O)CH_2 + O_2 + M \rightarrow CH_3C(O)CH_2O_2 \qquad (24)$$

The acetonylperoxy radical ($CH_3C(O)CH_2O_2$) can react with NO[44] to form $CH_3C(O)CH_2O$, the fate of which is reaction 25 to form $CH_3C(O)$ and HCHO.[45]

$$CH_3C(O)CH_2O + M \rightarrow CH_3C(O) + HCHO + M \qquad (25)$$

$$CH_3C(O) + O_2 + M \rightarrow CH_3C(O)O_2 + M \qquad (14)$$

As the CH_3 radical that is directly formed in the photolysis of $CH_3C(O)CH_3$ is largely converted to HCHO (reactions 13, 17, and 18) in the presence of sufficient NO_x, the net result of reaction by H-abstraction by OH is formation of two HCHO, but (excluding subsequent HCHO degradation) no net production of OH. Also, four NO are oxidized to NO_2 via this mechanism.

On the other hand, the reaction with NO_2 can form peroxyacetonyl nitrate:

$$CH_3C(O)CH_2O_2 + NO_2 + M \rightarrow CH_3C(O)CH_2O_2NO_2 + M \qquad (26)$$

which may have a lifetime of 1 day or longer close to the tropopause, but unlike PAN is not sufficiently stable to provide a mechanism for the long-range transport of NO_x.[44]

Our kinetic data indicate, however, that a substantial proportion of the reaction of OH with acetone may proceed via complex formation, which may result in formation of $CH_3C(O)OH$ and CH_3 products, especially at low temperatures.

$$CH_3C(O)CH_3 + OH \rightarrow CH_3 + CH_3C(O)OH \qquad (1b)$$

The net result of the oxidation of acetone by reaction 1b is the formation of only one HCHO, one molecule of $CH_3C(O)OH$, the oxidation of just two NO to NO_2, and no net OH formation apart from that which results from the transformation of CH_3 radicals to HCHO and its subsequent oxidation. In this case, PAN formation will also be substantially reduced as the acetyl group $CH_3C(O)$ is tied up in acetic acid ($CH_3C(O)OH$), which is neither rapidly photolyzed nor reacts rapidly enough with OH to return the $CH_3C(O)$ radical on a short time scale.

Previous observations of high levels (up to 3 nmol/mol) of $CH_3C(O)OH$ in the upper troposphere are presently unexplained,[46] as the only known source of $CH_3C(O)OH$ (reaction 23b) is reduced in importance in the upper troposphere by the presence of NO_x which favors reaction of $CH_3C(O)O_2$ and HO_2 with NO and NO_2. Assuming that $CH_3C(O)OH$ is formed only in the reaction of OH with $CH_3C(O)CH_3$ and is lost only by reaction with OH, its steady-state concentration may be estimated as

$$[CH_3C(O)OH] = k_1[CH_3C(O)CH_3]\alpha/k_{27} \qquad (27)$$

where k_{27} is the rate constant for reaction of $CH_3C(O)OH$ with OH and is equal to 1×10^{-12} cm^3 s^{-1} at 210 K[32] and α is the branching ratio to $CH_3C(O)OH$ formation.

$$OH + CH_3C(O)OH \rightarrow \text{products} \qquad (27)$$

Assuming 1 nmol/mol of $CH_3C(O)CH_3$ and $\alpha = 1$, this expression results in acetic acid concentrations of $\approx$0.3 nmol/mol.

5. Conclusions

The rate coefficient for the reaction of OH with $CH_3C(O)CH_3$ was determined using pulsed laser photolytic generation of OH combined with fluorescence detection in real time. The data obtained indicate an increasing rate coefficient with increasing T above $\approx$240 K, and the reverse behavior between 202 and 240 K. The overall rate coefficient is given by k_1 (202−395 K) $= 8.8 \times 10^{-12} \exp(-1320/T) + 1.7 \times 10^{-14} \exp(423/T)$ cm^3 s^{-1}, which results in a significantly higher rate constant at the low temperatures of the upper troposphere than presently recommended. The formation of an association complex is a potential explanation for this behavior, and the possible formation of acetic acid (and CH_3) via decomposition of this association complex is discussed. In light of the present results, experiments that examine the formation of acetic acid in the low temperature OH-initiated oxidation of $CH_3C(O)CH_3$ and modeling exercises that reevaluate the role of $CH_3C(O)CH_3$ in the chemistry of the upper troposphere are required.

Acknowledgment. We gratefully acknowledge partial financial support within the BMBF-COACH project (01 LS 9801/3).

References and Notes

(1) Crutzen, P. J. Atmospheric interactions-homogeneous gas reactions of C, N, and S containing compounds. In *The major biogeochemical cycles and their interactions*; Bolin, B., Cook, R. B., Eds.; J. Wiley: Chichester, New York, 1983; p 67.

(2) Kanakidou, M.; Singh, H. B.; Valentin, K. M.; Crutzen, P. J. *J. Geophys. Res.* **1991**, *96*, 15395.

(3) Singh, H. B.; Hanst, P. L. *Geophys. Res. Lett.* **1981**, *8*, 941.

(4) Chatfield, R. B.; Gardner, E. P.; Calvert, J. G. *J. Geophys. Res.* **1987**, *92*, 4208.

(5) Singh, H. B.; O'Hara, D.; Herlth, D.; Sachse, W.; Blake, D. R.; Bradshaw, J. D.; Kanakidou, M.; Crutzen, P. J. *J. Geophys. Res.* **1994**, *99*, 1805.

(6) Warneke, C.; Karl, T.; Judmaier, H.; Hansel, A.; Jordan, A.; Lindinger, W.; Crutzen, P. J. *Global Biogeochem. Cycles* **1999**, *13*, 9.

(7) Holzinger, R.; Warneke, C.; Hansel, A.; Jordan, A.; Lindinger, W.; Scharffe, D.; Schade, G.; Crutzen, P. J. *Geophys. Res. Lett.* **1999**, *26*, 1161.

(8) Knop, G.; Arnold, F. *Geophys. Res. Lett.* **1987**, *14*, 1262.

(9) Singh, H. B.; Kanakidou, M.; Crutzen, P. J.; Jacob, D. J. *Nature* **1995**, *378*, 50.

(10) Arnold, F.; Schneider, J.; Gollinger, K.; Schlager, H.; Schulte, P.; Hagen, D. E.; Whitefield, P. D.; van Velthoven, P. *Geophys. Res. Lett.* **1997**, *24*, 57.

(11) Arnold, F.; Bürger, V.; Droste-Fanke, B.; Grimm, F.; Krieger, A.; Schneider, J.; Stilp, T. *Geophys. Res. Lett.* **1997**, *24*, 3017.

(12) Pöschl, U.; Williams, J.; Hoor, P.; Fischer, H.; Crutzen, P. J.; Warneke, C.; Holzinger, R.; Hansel, A.; Jordan, A.; Lindinger, W.; Scheeren, H. A.; Peters, W.; Lelieveld, J. *J. Atmos. Chem.*, in press.

(13) Singh, H. B.; Chen, Y.; Gregory, G. L.; Sachse, G. W.; Talbot, R.; Blake, D. R.; Kondo, Y.; Bradshaw, J. D.; Heikes, B.; Thornton, D. *Geophys. Res. Lett.* **1997**, *24*, 127.

(14) Jaeglé, L.; Jacob, D. J.; Brune, W. H.; Tan, D.; Faloona, I. C.; Weinheimer, A. J.; Ridley, B. A.; Campos, T. L.; Sachse, G. W. *Geophys. Res. Lett.* **1998**, *25*, 1709.

(15) Wennberg, P. O.; Hanisco, T. F.; Jaeglé, L.; Jacob, D. J.; Hintsa, E. J.; Lanzendorf, E. J.; Anderson, J. G.; Gao, R.-S.; Keim, E. R.; Donnelly, S. G.; Del Negro, L. A.; Fahey, D. W.; McKeen, S. A.; Salawitch, R. J.; Webster, C. R.; May, R. D.; Herman, R. L.; Proffitt, M. H.; Margitan, J. J.; Atlas, E. L.; Schauffler, S. M.; Flocke, F.; McElroy, C. T.; Bui, T. P. *Science* **1997**, *279*, 49.

(16) Folkins, I.; Wennberg, P. O.; Hanisco, T. F.; Anderson, J. G.; Salawitch, R. J. *Geophys. Res. Lett.* **1997**, *24*, 3185.

(17) Crowley, J. N.; Campuzano-Jost, P.; Moortgat, G. K. *J. Phys. Chem.* **1996**, *100*, 3601.

(18) Crowley, J. N.; Carl, S. A. *J. Phys. Chem. A* **1997**, *101*, 4178.

(19) Carl, S. A.; Crowley, J. N. *J. Phys. Chem. A* **1998**, *102*, 8131.

(20) Hughes, K. J.; Pereira, A. R.; Pilling, M. J. *Ber. Bunsen Ges. Phys. Chem.* **1992**, *96*, 1352.

(21) Tsang, W.; Hampson, R. F. *J. Phys. Chem. Ref. Data* **1986**, *15*, 1087.

(22) Burkholder, J. B.; Mellouki, A.; Talukdar, R.; Ravishankara, A. R. *Int. J. Chem. Kinet.* **1992**, *24*, 711.

(23) Vaghjiani, G. *J. Chem. Phys.* **1993**, *99*, 5936.

(24) Wine, P. H.; Nicovich, J. M.; Hynes, A. J.; Wells, J. R. *J. Phys. Chem.* **1986**, *90*, 4033.

(25) Dieke, G. H.; Crosswhite, H. M. *J. Quantum Spec. Radiat. Transfer* **1962**, *2*, 97.

(26) Calvert, J. G.; Pitts, J. N. J. *Photochemistry*; J. Wiley: New York, 1966.

(27) Meyrahn, H.; Pauly, J.; Schneider, W.; Warneck, P. *J. Atmos. Chem.* **1986**, *4*, 277.

(28) Hynes, A. J.; Kenyon, E. A.; Pounds, A. J.; Wine, P. H. *Spectrochim. Acta* **1992**, *48A*, 1235.

(29) Gierczak, T.; Burkholder, J. B.; Bauerle, S.; Ravishankara, A. R. *Chem. Phys.* **1998**, *231*, 229.

(30) Martinez, R. D.; Buitrago, A. A.; Howell, N. W.; Hearn, C. H.; Joens, J. A. *Atmos. Environ.* **1992**, *26A*, 785.

(31) Herron, J. T. *J. Phys. Chem. Ref. Data* **1988**, *17*, 967.

(32) DeMore, W. B.; Sander, S. P.; Golden, D. M.; Hampson, R. F.; Kurylo, M. J.; Howard, C. J.; Ravishankara, A. R.; Kolb, C. E.; Molina, M. J. Chemical Kinetics and Photochemical Data for Use in Stratospheric Modelling, No 11; Jet Propulsion Laboratory: Pasadena, CA, 1997.

(33) Le Calvé, S.; Hitier, D.; Le Bras, G.; Mellouki, A. *J. Phys. Chem. A* **1998**, *102*, 4597.

(34) Wallington, T. J.; Kurylo, M. J. *J. Phys. Chem.* **1987**, *91*, 5050.

(35) Atkinson, R.; Baulch, D. L.; Cox, R. A.; Hampson, R. F.; Jr; Kerr, J. A.; Troe, J. *J. Phys. Chem. Ref. Data* **1992**, *21*, 1125.

(36) Zetzsch, C. Rate constants for the reactions of OH with acetone and methylethyl ketone in the gas phase. 7th International symposium on gas kinetics, 1982, Göttingen, Germany.

(37) Cox, R. A.; Derwent, R. G.; Williams, M. R. *Environ. Sci. Technol.* **1980**, *14*, 57.

(38) Kerr, J. A.; Stocker, D. W. *J. Atmos. Chem.* **1986**, *4*, 253.

(39) Chiorboli, C.; Bignozzi, C. A.; Maldotti, A.; Giardini, P. F.; Rossi, A.; Carassiti, V. *Int. J. Chem. Kinet.* **1983**, *15*, 579.

(40) Bott, J. F.; Cohen, N. *Int. J. Chem. Kinet.* **1991**, *23*, 1017.

(41) McKeen, S. A.; Gierzak, T.; Burkholder, J. B.; Wennberg, P. O.; Hanisco, T. F.; Keim, E. R.; Gao, R.-S.; Liu, S. C.; Ravishankara, A. R.; Fahey, D. W. *Geophys. Res. Lett.* **1997**, *24*, 3177.

(42) Folkins, I.; Chatfield, R.; Singh, H.; Chen, Y.; Heikes, B. *Geophys. Res. Lett.* **1998**, *25*, 1305.

(43) Prather, M. J.; Jacob, D. J. *Geophys. Res. Lett.* **1997**, *24*, 3189.

(44) Sehested, J.; Christensen, L. K.; Nielsen, O. J.; Bilde, M.; Wallington, T. J.; Schneider, W. F.; Orlando, J. J.; Tyndall, G. S. *Int. J. Chem. Kinet.* **1998**, *30*, 475.

(45) Jenkin, M. E.; Cox, R. A.; Emrich, M.; Moortgat, G. K. *J. Chem. Soc., Faraday Trans.* **1993**, *89*, 2983.

(46) Jacob, D. J.; Heikes, B. G.; Fan, S.-M.; Logan, J. A.; Mauzerall, D. L.; Bradshaw, J. D.; Singh, H. B.; Gregory, G. L.; Talbot, R. W.; Blake, D. R.; Sachse, G. W. *J. Geophys. Res.* **1996**, *101*, 24235.